

Diffuse γ -ray emission around the massive star forming region of Carina Nebula Complex

Ting-Ting Ge¹, Xiao-Na Sun^{1*}, Rui-Zhi Yang^{2,3,4}, Yun-Feng Liang¹, En-Wei Liang¹

¹Guangxi Key Laboratory for Relativistic Astrophysics, School of Physical Science and Technology, Guangxi University, Nanning 530004, China

²Department of Astronomy, School of Physical Sciences, University of Science and Technology of China, Hefei, Anhui 230026, China

³CAS Key Laboratory for Research in Galaxies and Cosmology, University of Science and Technology of China, Hefei, Anhui 230026, China

⁴School of Astronomy and Space Science, University of Science and Technology of China, Hefei, Anhui 230026, China

5 October 2022

ABSTRACT

We report the Fermi Large Area Telescope (*Fermi*-LAT) detection of the γ -ray emission toward the massive star forming region of Carina Nebula Complex (CNC). Using the latest source catalog and diffuse background models, we found that the GeV γ -ray emission in this region can be resolved into three different components. The GeV γ -ray emission from the central point source is considered to originate from the η Carina (η Car). We further found the diffuse GeV γ -ray emission around the CNC which can be modelled by two Gaussian disks with radii of 0.4° (region A) and 0.75° (region B), respectively. The GeV γ -ray emission from both the regions A and B have good spatial consistency with the derived molecular gas in projection on the sky. The GeV γ -ray emission of region A reveals a characteristic spectral shape of the pion-decay process, which indicates that the γ -rays are produced by the interactions of hadronic cosmic rays with ambient gas. The γ -rays spectrum of region B has a hard photon index of 2.12 ± 0.02 , which is similar to other young massive star clusters. We argue that the diffuse GeV γ -ray emission in region A and region B likely originate from the interaction of accelerated protons in clusters with the ambient gas.

Key words: cosmic rays – gamma-rays: ISM - open clusters and associations: individual: CNC

1 INTRODUCTION

The origin of cosmic rays (CRs) in the Milky Way is still a mystery. Supernova remnants (SNRs) have long been considered as the main acceleration sites of Galactic CRs (Baade & Zwicky 1934). Moreover, growing evidence suggests that the young massive star clusters (YMCs) play an important role in accelerating Galactic CRs. Several such systems have been identified, e.g., Cygnus cocoon (Ackermann et al. 2011; Aharonian et al. 2019), Westerlund 1 (Abramowski et al. 2012), Westerlund 2 (Yang et al. 2018), NGC 3603 (Yang & Aharonian 2017), 30 Dor C (H.E.S.S. Collaboration et al. 2015), RSGC 1 (Sun et al. 2020a), W40 (Sun et al. 2020b), Mc20 (Sun et al. 2022), and NGC 6618 (Liu et al. 2022).

CNC is one of the most active and nearest massive star forming regions in our Galaxy. It is located in the Carina spiral arm (Vallée 2014) with the distance of ~ 2.3 kpc (Smith & Brooks 2007). It contains 8 open clusters with more than 66 O-type stars, 3 Wolf-Rayet (WR) stars, and the peculiar object of the Luminous Blue Variable (LBV) η Car (Smith 2008). Potential particle acceleration sites in

the CNC include massive binary systems (e.g., η Car), massive star clusters (e.g., Tr 14, 15, 16), and possibly some unrecognized SNRs (Smith et al. 2000). The central region of CNC mainly consists of the young star clusters Tr 14, 15, and 16. The northwestern part of CNC contains prominent ionized hydrogen (H II) region Gum 31 around the very young (~ 1 -2 Myr) stellar cluster NGC 3324, and the oldest (~ 8 -10 Myr) cluster NGC 3293 (Göppel & Preibisch 2022; Preibisch et al. 2017). Tr 14 is one of the most extensively studied young (~ 1 Myr) massive clusters in our Galaxy. It contains no less than 13 O-type stars, and its total mass is estimated to be $1 \times 10^4 M_\odot$ (Ascenso et al. 2007). Tr 14 may be 1-2 Myr younger than Tr 16 (Smith 2006), and is closer to its associated molecular cloud than Tr 16 (?). Tr 16 includes 42 O-type stars. It is well-known for the presence of η Car, which is a massive, variable star binary. η Car is composed of a primary star (a LBV star with more than $90 M_\odot$) and a companion star (an O or WR star with less than $30 M_\odot$) (Hillier et al. 2001; Verner et al. 2005). Both stars in η Car have strong winds and high mass-loss rates. The stellar mass-loss rate of the primary is $\dot{M}_1 \approx 2.5 \times 10^{-4} M_\odot \text{ yr}^{-1}$ with terminal velocity of 500 km s^{-1} (Pittard & Corcoran 2002). The companion star has a stellar mass-loss rate of $\dot{M}_2 \approx 10^{-5} M_\odot \text{ yr}^{-1}$ and faster stellar wind with terminal velocity of 3000 km s^{-1} (Pittard & Corcoran 2002; Parkin et al. 2009). In colliding-wind

* E-mail: xiaonasun@gxu.edu.cn

binaries (CWBs) or YMCs, strong shocks produced by the interaction between their powerful stellar winds which interacts with the interstellar medium likely accelerate particles to very high energy (Del Valle & Romero 2012; De Becker & Raucaq 2013). X-rays observations with *NuSTAR* (Hamaguchi et al. 2018) and γ -rays observations (White et al. 2020) show that the accelerated particles produce non-thermal emission through colliding with surrounding gas.

The Astro-Rivelatore Gamma a Immagini Leggero (*AGILE*) (Tavani et al. 2009) and *Fermi*-LAT (Abdo et al. 2009a) have detected γ -ray emissions from the direction of η Car. Its γ -ray spectrum measured using *Fermi*-LAT can be described by two different components with a division of 10 GeV. The high-energy component is generally suggested to be the hadronic origin (Farnier et al. 2011; Reitberger et al. 2015; Balbo & Walter 2017; White et al. 2020). The origin of the lower-energy component is still uncertain (Farnier et al. 2011; Gupta & Razaque 2017; Balbo & Walter 2017; Ohm et al. 2015; White et al. 2020). Recently, a point-like VHE γ -ray source from the direction of η Car was detected by HESS. Its spectrum is described by a power-law. (H. E. S. S. Collaboration et al. 2020).

For GeV γ -ray emission, η Car is considered as a point-like source. Until recently, White et al. (2020) found significant extended γ -ray emission around the η Car, and they use a CO template of this region to model the extended emission. Yang et al. (2018) analyzed the origin of the γ -ray emission from FGES J1036.3-5833 which includes the regions of Westerlund 2 and CNC. FGES J1023.3-5747 (Ackermann et al. 2017) and HESS J1023-575 (Aharonian et al. 2007; H. E. S. S. Collaboration et al. 2011) are the diffuse γ -ray emission seen from the vicinity of Westerlund 2 (Yang et al. 2018; Mestre et al. 2021) which seem to indicate that the YMC Westerlund 2 can provide sufficient non-thermal energy to account for the γ -ray emission.

In this paper, we analyzed the γ -ray emission toward CNC taking advantage of more than 13 years of *Fermi*-LAT data, and tried to study the possible origin of CNC γ -ray emission. The paper is organized as follows. In Sect.2, we present the data set and the results of the data analysis. In Sect.3, we study the gas distributions in this region. In Sect.4, we investigate the possible origin of the γ -ray emissions. In Sect.5, the CR content around this region is discussed. Finally, In Sect.6, we discuss the implications of our results.

2 *Fermi*-LAT DATA ANALYSIS

We selected the latest *Fermi*-LAT Pass 8 data around the CNC region from August 4, 2008 (MET 239557417) until September 25, 2021 (MET 654297860), and used the standard LAT analysis software package *v11r5p3*¹. We chose a $10^\circ \times 10^\circ$ square region centered at the position of CNC (R.A. = 161.00°, Dec. = -59.55°) as the region of interest (ROI). The instrument response functions (IRFs) *P8R3_SOURCE_V3* was selected to analyze the events in the ROI of *evtype* = 3 and *evclass* = 128. We also applied the recommended expression (*DATA_QUAL* > 0) && (*LAT_CONFIG* == 1) to select the good time intervals (GTIs) based on the information provided in the spacecraft file. In order to reduce γ -ray contamination from the Earth's albedo, only the events with zenith angles less than 90° are

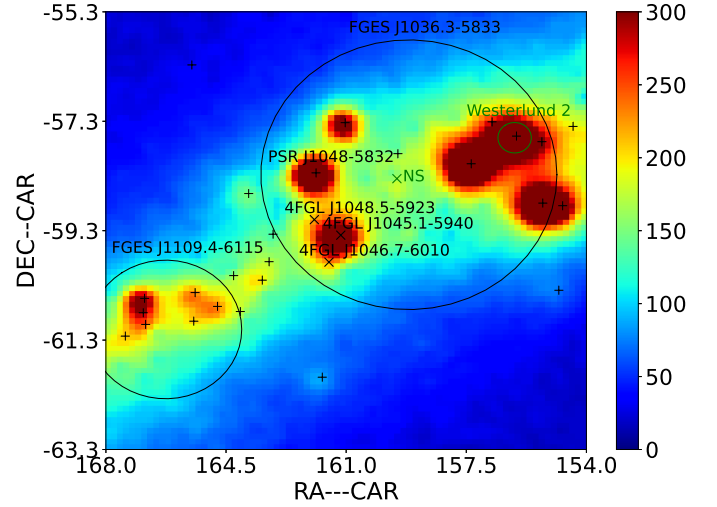


Figure 1. *Fermi*-LAT counts map above 500 MeV in the $8^\circ \times 8^\circ$ region surrounding the CNC, with pixel size of $0.1^\circ \times 0.1^\circ$. All black pluses represent the 4FGL-DR2 sources within the region. The black circle shows the extended emission related to FGES J1036.4-5833. The green circle shows the YMCs Westerlund 2. The crosses indicate the three point sources 4FGL J1045.1-5940, 4FGL J1048.5-5923, 4FGL J1046.7-6010 around the CNC.

included for the analysis. We used the Python module that implements a maximum likelihood optimization technique for a standard binned analysis².

In the background model, we included the recently released *Fermi*-LAT 10-year Source Catalog (4FGL-DR2, Ballet et al. 2020; Abdollahi et al. 2020) within the ROI enlarged by 5° . The source model file was generated using the script *make4FGLxml.py*³, and all sources within 4.5° of center were set free. For the diffuse background components, we use the latest Galactic diffuse emission model *gll_iem_v07.fits* and isotropic extragalactic emission model *iso_P8R3_SOURCE_V3_v1.txt*⁴ with their normalization parameters free.

First, we used the events above 500 MeV to study the spatial distribution of the γ -ray emission near CNC. The γ -ray counts map in the $8^\circ \times 8^\circ$ region around CNC is shown in Fig.1. In our analysis, we found a new source of which the TS and corresponding position are (TS = 129; l = 285.29; b = 0.15). It is marked with green cross in Fig.1. We find no counterpart for this new source in other wavelengths. We put the new source in the spatial analysis model with a power-law spectrum. In addition, Martí-Devesa & Reimer (2021) found a new source (i.e. 4FGL J 1036.1-5934) identified as the nova that occurred in March 2018 (Jean et al. 2018). This new source is also included in the latest catalog. Thus, to prevent contamination at the position of CNC from the emission of nova, we excluded the data from MET 542636972 to 558588527. We note that there are three 4FGL-DR2 catalog point sources: 4FGL J1045.1-5940, 4FGL J1048.5-5923, 4FGL J1046.7-6010. 4FGL J1045.1-5940 was identified as the massive binary η Car.

² https://fermi.gsfc.nasa.gov/ssc/data/analysis/scitools/python_tutorial/

³ <https://fermi.gsfc.nasa.gov/ssc/data/analysis/user/>

⁴ <https://fermi.gsfc.nasa.gov/ssc/data/access/lat/BackgroundModels.html>

¹ <https://fermi.gsfc.nasa.gov/ssc/data/analysis/software/>

2.1 Multi-point source model

To study the excess γ -ray emission around CNC, we test several different models. The tested models are summarized in Table 1. We firstly determine a point source that used to model η Car binary stars. To do that, we excluded these three point sources from our background model. We added a point-like source at the η Car's position into our background model, and optimized the localization using the *gfindsrc* tool. The best-fit position of the excess above 500 MeV is [RA = 161.30°, Dec = -59.70°], with 2σ error radius of 0.15°. In the later analysis, the point source at this position (source η Car) will be always included in the models and is used to represent the emission from η Car. Our first model (model 1) use three point sources (point source η Car, 4FGL J1046.7-6010 and 4FGL J1048.5-5923) to model the excess γ -ray emission around CNC. Each point source has a LogParabola spectral shape. We performed a binned likelihood analysis to derive the likelihood value ($-\log(\mathcal{L})$) and the Akaike information criterion (AIC, Akaike (1974)) value. The AIC is defined as $AIC = -2\log(\mathcal{L}) + 2k$, where k is the number of free parameters in the model. The derived $-\log(\mathcal{L})$ and AIC for the multi-point source model are -1265307 and -2530414, respectively.

2.2 Spatial template for two Gaussian disks

To further investigate the diffusion of the GeV γ -ray emission, we used a spatial template that consists of two regions (A, B). Each region are modelled as a Gaussian disk and we varied the positions and sizes of the disks to find the best-fit parameters. The significance of the extended source is quantified by $TS_{\text{ext}} = 2\log(\mathcal{L}_{\text{ext}}/\mathcal{L}_{\text{ps}})$, where \mathcal{L}_{ext} is the maximum likelihood for the extended source model, and \mathcal{L}_{ps} for the point-like sources model (Lande et al. 2012). For region A, we found that the γ -ray emission of η Car is very strong. Hence, the added the center of Gaussian disk is set at above best-fit position. The radius of the disk varies from 0.2° to 1° in steps of 0.05°. We used this Gaussian disks to replace the spatial components of the two unassociated point sources: 4FGL J1046.7-6010 and 4FGL J1048.5-5923 in the multi-point source model. The likelihood ratio peak at the Gaussian disk template with a radius of $0.4^\circ \pm 0.02^\circ$ can fit the γ -ray excess for the central part of the CNC (region A).

It was found that there exists extended residual γ -ray emission in the northwestern part of the CNC (region B) after this process. Therefore, to find out whether the residual emission is extended or not, we used a point-like source or a Gaussian disk to model this residuals. The position of the added point source or the center of the Gaussian disk is set to the peak position of the residuals. The tested radius of the Gaussian disk varies from 0.2° to 1° with a step of 0.05 for region B. In the above test, we find that the Gaussian disks with the radii of 0.75° for the region B and 0.4° for the region A (model 2) can best fit the data. The derived $-\log(\mathcal{L})$ and AIC for this model are -1265580 and -2530978, respectively. We subtracted the 0.4° Gaussian disk and the 0.75° Gaussian disk from the model 2 and derived the residual map shown in Fig. 2. The map revealed significant diffuse residuals in this region. In the following subsections, we test different spatial models of these diffuse emissions.

2.3 Spatial template for molecular hydrogen

To determine whether the extended GeV γ -ray emission is correlated with the gas distribution, we considered a spatial template of

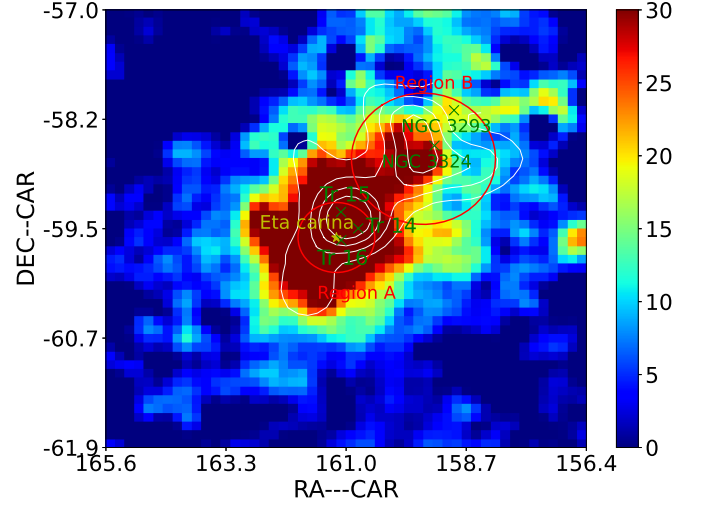


Figure 2. Residual map above 500 MeV near the CNC after subtracting two Gaussian disks with a radii of 0.4° and 0.75° from the model 2. Details are given in Sect. 2.2. The map has a size of $5^\circ \times 5^\circ$ ($0.1^\circ \times 0.1^\circ$ pixelsize) and has been smoothed with a Gaussian kernel of 0.9°. The regions A and B is marked with the red circles. The green crosses indicate the star clusters. The yellow asterisk indicates the position of η Car. The white contours show the H_2 column density derived in Sect. 3.

H_2 . For the H_2 template, we use the Carbon monoxide (CO) composite survey (see Sect. 3 for details) to produce. As shown in Fig. 2, the white contours represent the H_2 distribution from the CO measurements, which overlap well with the excess emission. We added the H_2 template (with a power-law spectrum) into the multi-point source model to obtain our model 3. Through the binned likelihood analysis, the derived $-\log(\mathcal{L})$ and the AIC for the H_2 template are -1265540 and -2530890, respectively.

2.4 Spatial template for molecular and ionized hydrogen

CNC contains one of the largest and most active $H\text{ II}$ regions in our Galaxy. The derivation for the details of the $H\text{ II}$ distribution is given in Sect. 3. We also note that the γ -ray emission has good spatially correlation with the $H\text{ II}$ gas (see Sect. 3). Thus, we adopted a spatial template considering $H\text{ II} + H_2$ gases. We summed the column density of $H\text{ II}$ and H_2 gases to generate the $H_2 + H\text{ II}$ template with a power-law spectral shape. The $H_2 + H\text{ II}$ template is added into the multi-point source model as a diffuse component (model 4). After performing the binned likelihood analysis, the derived $-\log(\mathcal{L})$ and the AIC for the spatial model of $H_2 + H\text{ II}$ are -1265619 and -2531048, respectively.

2.5 Spatial template for two Gaussian disks and multi-point sources

In the model 2, we removed the two point sources 4FGL J1046.7-6010 and 4FGL J1048.5-5923 from the background and accounted for the emissions close to CNC with extended components. Here we further test the inclusion of both the extended components and two point sources in the model (model 5). Thus, we added the two 4FGL point sources back into the model file based on the model 2. Each point source has a LogParabola spectral shape. We find that this model (multi-point sources + 0.4° + 0.75° Gaussian disks), can explain the observational data best among the 5 models we have

Table 1. Spatial analysis (>500MeV) results for the different models.

Model	$-\log(\mathcal{L})$	TS_{ext}	d.o.f.	ΔAIC
Model 1 (multi-point sources)	-1265277	-	93	-
Model 2 (0.4° Gaussian disk + 0.75° Gaussian disk)	-1265580	606	91	-610
Model 3 (multi-point sources + H_2 template)	-1265540	526	95	-522
Model 4 (multi-point sources + H_2 + $H\text{ II}$ template)	-1265619	684	95	-680
Model 5 (multi-point sources + 0.4° Gaussian disk + 0.75° Gaussian disk)	-1265647	740	97	-732

considered. The derived $-\log(\mathcal{L})$ for model 5 is equal to -1265647, and the AIC is equal to -2531100.

To compare the goodness of the fit in the different models, we also calculated the ΔAIC , the AIC of the model 1 and the model 2-5. It is evident from Table 1 that the model with the two Gaussian disks and multi-point sources provides the highest TS_{ext} value and the minimum ΔAIC value. Therefore, in the following analysis, we use the model 5 as the spatial template.

The derived photon index for 0.4° Gaussian disk above 500 MeV is 2.36 ± 0.01 and the total γ -ray flux can be estimated as $(2.65 \pm 0.02) \times 10^{-8} \text{ ph cm}^{-2} \text{ s}^{-1}$. Considering the distance of about 2.3 kpc, the total γ -ray luminosity is estimated to be $(1.34 \pm 0.01) \times 10^{34} \text{ erg s}^{-1}$ above 500 MeV with the single power-law spectrum. The photon index of 0.75° Gaussian disk is 2.12 ± 0.02 and the total flux is estimated as $(1.97 \pm 0.02) \times 10^{-8} \text{ ph cm}^{-2} \text{ s}^{-1}$, corresponding to $(9.95 \pm 0.08) \times 10^{33} \text{ erg s}^{-1}$ above 500 MeV. We found that this model give the best log-likelihood value. We argue these additional point sources may represent the contamination from bright central source η Car. In our following spectral analysis we derive the spectral energy distributions (SEDs) of the two Gaussian disks with and without the additional multiple point sources (model 2 and model 5), respectively. We found the results are consistent with each other within error bars. And we include the difference as systematic errors.

2.6 Spectral analyses

We used the best-fit spatial template as the spatial model of the extended γ -ray emission, and assumed a power-law spectral shape to extract the SED. We divided the energy range 300 MeV-200 GeV into seven logarithmically spaced energy bins, and in each bin the SED flux is derived via the maximum-likelihood method. We calculated the upper limits within 3σ for the energy bins with a significance lower than 2σ . Fig.3 shows the derived SEDs of the regions A (black) and B (red). The dashed line represents the predicted γ -ray emissions assuming the CR density in regions A and B, respectively. In the analysis, we estimated the uncertainties of SEDs system due to the Galactic diffuse emission model and the LAT effective area (A_{eff}) by changing the normalization by $\pm 6\%$ from the best-fit value for each energy bins, and considered the maximum flux deviations of the source as the systematic error (Abdo et al. 2009b).

3 GAS CONTENT AROUND CNC

We investigated three different gas phases, i.e., the H_2 , the neutral atomic hydrogen ($H\text{ I}$), and the $H\text{ II}$, in the vicinity of CNC region.

The $H\text{ I}$ data is from the data-cube of the $H\text{ I}$ 4π survey (HI4PI), which is a 21-cm all-sky database of Galactic $H\text{ I}$

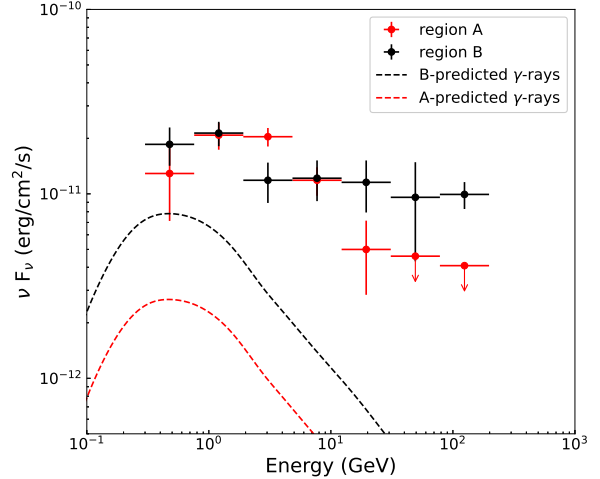


Figure 3. SEDs of γ -ray emission in the region A (black point) and region B (red data) based on the model 5. The dashed curves represent the predicted γ -ray emission assuming the CR density in the two regions is the same as those measured locally by AMS-02 (Aguilar et al. 2015). Both the statistical and systematic errors are considered. For details, see the context in Sect. 2.6.

(HI4PI Collaboration et al. 2016). We estimated the $H\text{ I}$ column density using the equation,

$$N_{H\text{ I}} = -1.83 \times 10^{18} T_s \int dv \ln \left(1 - \frac{T_B}{T_s - T_{\text{bg}}} \right), \quad (1)$$

where $T_{\text{bg}} \approx 2.66$ K is the brightness temperature of the cosmic microwave background radiation at 21 cm, and T_B is the brightness temperature of the $H\text{ I}$ emission. In the case when $T_B > T_s - 5$ K, we truncate T_B to $T_s - 5$ K; T_s is chosen to be 150 K. The derived $H\text{ I}$ column map integrated in the velocity range $v_{\text{LSR}} = [-32, -5]$ km s^{-1} (Seo et al. 2019; Rebolledo et al. 2021) is shown in the left panel of Fig.4. We also use this range to integrate the line emission of the CO in this velocity range.

We use the CO composite survey (Dame et al. 2001) to trace the H_2 . The standard assumption of a linear relationship between the velocity-integrated brightness temperature of CO 2.6-mm line, W_{CO} , and the column density of molecular hydrogen, $N(H_2)$, i.e., $N(H_2) = X_{\text{CO}} \times W_{\text{CO}}$ (Lebrun et al. 1983). X_{CO} is the H_2/CO conversion factor that chosen to be $2.0 \times 10^{20} \text{ cm}^{-2} \text{ K}^{-1} \text{ km}^{-1} \text{ s}$ as suggested by Dame et al. (2001) and Bolatto et al. (2013). The derived molecular gas column density is shown in the middle panel of Fig.4.

CNC is one of the largest and most active $H\text{ II}$ regions in the Galaxy. To obtain the $H\text{ II}$ column density we used the *Planck* free-free map (Planck Collaboration et al. 2016). First, we transformed the emission measure (EM) into free-free intensity by using the conversion factor in Table 1 of Finkbeiner (2003). Then, we calculate the $H\text{ II}$ column density from the intensity (I_ν) of free-free emission

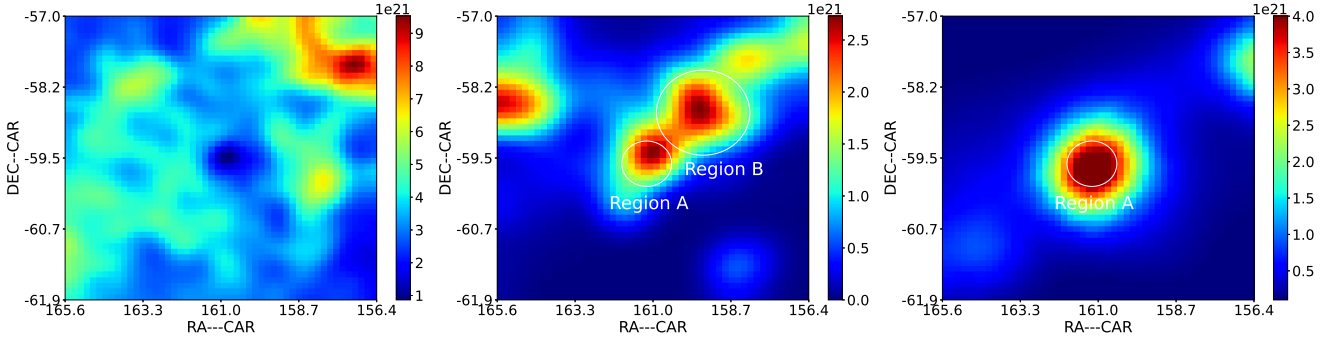


Figure 4. Maps of gas column densities in three gas phases. Left shows the map of H I column density derived from 21-cm all-sky survey. Middle shows the H₂ column density derived from the CO data. Right shows the H II column density derived from the *Planck* free-free map assuming the effective density of electrons $n_e = 10 \text{ cm}^{-3}$. The white circles indicate the region A and region B, which is the same as the red circles in Fig. 2. For details, see the context in Sect. 3.

Table 2. Gas total masses and number densities within the region A and region B. See Sect. 3 for details.

Tracer	Region	Mass ($10^4 M_\odot$)	Number density (cm^{-3})
H ₂ + H II	A	5.54 + 4.31	231
H ₂ + H II	B	16.18 + 3.99	72

by using Eq.(5) of [Sodroski et al. \(1997\)](#),

$$N_{\text{H II}} = 1.2 \times 10^{15} \text{ cm}^{-2} \left(\frac{T_e}{1 \text{ K}} \right)^{0.35} \left(\frac{\nu}{1 \text{ GHz}} \right)^{0.1} \left(\frac{n_e}{1 \text{ cm}^{-3}} \right)^{-1} \times \frac{I_\nu}{1 \text{ Jy sr}^{-1}}, \quad (2)$$

where $\nu = 353 \text{ GHz}$ is the frequency, and an electron temperature of $T_e = 8000 \text{ K}$. The H II column density is inversely proportional to the effective density of electrons n_e . Thus, we adopted an effective density 10 cm^{-3} , which is the value suggested in [Sodroski et al. \(1997\)](#) for the region inside the solar circle. The derived H II column density is also shown in the right panel of Fig. 4. We note that the H II gas distribution is similar to that of the YMCs NGC 3603 ([Yang & Aharonian 2017](#)) and W40 ([Sun et al. 2020b](#)). They all have the γ -ray emission region, which shows good spatial consistency with the H II column density. Moreover, several YMCs are located here, i.e Tr 16, Tr 14, which had ionized the ambient media in the CNC.

The total mass within the cloud in each pixel can be calculated from the expression

$$M_{\text{H}} = m_{\text{H}} N_{\text{H}} A_{\text{angular}} d^2 \quad (3)$$

where M_{H} is the mass of the hydrogen atom, $N_{\text{H}} = N_{\text{H II}} + 2N_{\text{H}_2} + N_{\text{H I}}$ is the total column density of the hydrogen atom in each pixel. A_{angular} is the angular area, and d is the distance of CNC. The total mass in the GeV γ -ray emission region is estimated to be $\sim 5.54 \times 10^4 M_\odot$ for region A and $\sim 1.62 \times 10^5 M_\odot$ for region B. If we assume the GeV γ -ray emission within both the regions A and B are spherical in geometry, with the corresponding sizes of 0.4° and 0.75° . The radius can be estimated as $r_{\text{A,B}} = d \times \theta_{\text{A,B}}$ (rad), and d is the distance to the objective region. The averaged over the volume gas number density of region A is $n_{\text{gas}} = 231 \text{ cm}^{-3}$, while for region B, the values is $n_{\text{gas}} = 72 \text{ cm}^{-3}$. Table 2 shows the gas total masses and number densities within the region A and region B.

4 THE ORIGIN OF GAMMA-RAY EMISSION

There is the massive binary η Car in the center of region A. In spatial analysis, we added η Car in the background model as a point-like source. PSR J1048-5832 is located about 1.2° away from the center of the γ -ray emission region (as shown in Fig. 1), which makes the association of the diffuse γ -ray emission to this pulsar unlikely ([Danilenko et al. 2013](#)). On the other hand, there are no known SNRs inside this region.

4.1 Region A

[White et al. \(2020\)](#) found that the significant extended γ -ray emission in this region, suggesting an additional component associated with CRs interactions. In our case, the YMCs Tr 14 and Tr 16 are the most promising sources of the CRs. Although we cannot rule out the possibility that η Car is the source of the CRs that produced the diffuse γ -ray emissions, we postulate here that those clusters may be another natural acceleration site of the CRs. We used Naima⁵ ([Zabalza 2015](#)) to fit the SEDs. Naima is a numerical package that allows us to implement different functions and includes tools to perform Markov chain Monte Carlo (MCMC) fitting of nonthermal radiative processes to the data. We note that the extended GeV emission and the molecular hydrogen gas are spatially correlated. Thus, we assume the γ -rays are produced in the pion-decay process from the interaction of the CRs with the ambient molecular clouds. Because the low-energy data points are poorly constrained, we used a broken power-law spectrum

$$N(E) = \begin{cases} A(E/E_0)^{-\alpha_1} & : E < E_b \\ A(E_b/E_0)^{(\alpha_2 - \alpha_1)} (E/E_0)^{-\alpha_2} & : E > E_b \end{cases}, \quad (4)$$

to fit the GeV γ -ray data. The derived SED is shown in Fig. 5. We treated A , α_1 , α_2 , E_b as free parameters for the fitting. As calculated in this section, the average number densities of the target protons for regions A and B are 231 cm^{-3} and 72 cm^{-3} , respectively, which are derived from the gas distributions in Sect. 3 consider H₂ + H II. In Fig. 5, we present the best-fitting results for region A. The maximum log-likelihood value is -0.1. The derived parameters are $\alpha_1 = 0.9 \pm 0.3$, $\alpha_2 = 3.2^{+0.7}_{-0.3}$, $E_b = 21^{+4}_{-3} \text{ GeV}$ and the total energy is $W_p = (1.11 \pm 0.12) \times 10^{48} \text{ erg}$ for the protons above 2 GeV. The red dashed line in Fig. 5 represents the predicted the fluxes of γ -ray emissions based on the H₂ + H II column density

⁵ <https://naima.readthedocs.io/en/latest/index.html>

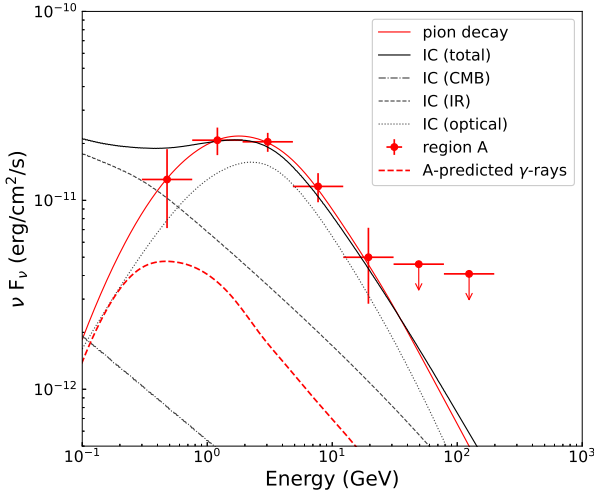


Figure 5. SED of emission in the region A for a 0.4° Gaussian disk spatial model. The red dashed line represents the predicted γ -ray emissions assuming the CR density in this region is the same as those measured locally by AMS-02 (Aguilar et al. 2015).

map in region A, assuming the CRs have the same as the local measurement by AMS-02 (Aguilar et al. 2015). We found that a significant CR enhancement in this region, which is predicted near the CR acceleration site.

We also tested the leptonic scenario that the γ -rays are generated via the inverse Compton (IC) scattering of relativistic electrons off the low-energy seed photons around this region. For the photon field of the IC calculations, we considered the cosmic microwave background (CMB) radiation field, optical-UV radiation field from the star light, and the dust infrared radiation field based on the model by Popescu et al. (2017). We note that region A is located in H II regions, the ionizing massive stars will increase the optical and UV fields significantly and thus produce additional IC emissions (Liu & Yang 2022). We calculated the IC spectrum using the formalism described in Khangulyan et al. (2014). To fit the lower energy break in the γ -ray spectrum, we require a relevant break in the spectrum of parent electrons. Thus, we assumed a broken power-law distribution of the relativistic electrons. As is shown in Fig.5, the solid black curve represents the total predicted γ -ray emission from the IC upscattering of the seed photons by relativistic electrons. The derived parameters for the electrons are $\alpha_1 = 0.51 \pm 0.1$, $\alpha_2 = 4.1^{+0.6}_{-0.4}$, $E_b = 15.3^{+3.0}_{-1.7}$ GeV and the total energy of the electrons (>2 GeV) is $W_e = (7.8 \pm 1.2) \times 10^{49}$ erg. The IC model can fit the observable data well, and the corresponding maximum-likelihood values is -0.91. We cannot formally rule out the leptonic origin of this region.

4.2 Region B

It should be noted that there is another possible particle accelerator located at the northwestern part of the CNC. For region B, including a bubble-shaped young H II region Gum 31 around the young stellar clusters NGC 3324, and NGC 3293 (Göppel & Preibisch 2022). Due to the good spatial correlation of the extended GeV γ -ray emission and the H_2 gas, it is very probable that the γ -rays are related to the H_2 gas. Thus, we used a hadronic scenario in which high energy γ -rays produced in the pion-decay process follow the proton-proton inelastic interactions, using the parameterization of the cross-section of

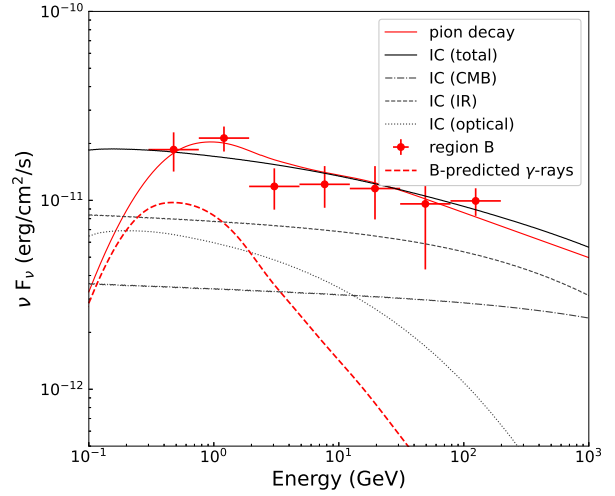


Figure 6. SED of emission in the region B for a 0.75° Gaussian disk spatial model. The red dashed line represents the predicted γ -ray emissions assuming the CR density in this region is the same as those measured locally by AMS-02 (Aguilar et al. 2015).

Kafexhiu et al. (2014). In this region, we used a single power-law spectrum for the parent proton distribution,

$$N(E) = A E^{-\alpha}, \quad (5)$$

treating A , α as free parameters for the fitting. As shown in Fig.6, we present the best-fit results for region B. The maximum log-likelihood value is -1.87. The derived index of the region B, $\alpha = 2.27 \pm 0.05$, with the total energy $W_p = (5.0 \pm 0.4) \times 10^{48}$ erg for the protons above 2 GeV.

In addition to the hadronic model, we also tried to consider a leptonic model where the γ -rays are from the IC scattering. We assume that the electrons have a single power-law spectrum. The target photon fields for relativistic electrons to scatter include the CMB, infrared, and optical field adopted from the local interstellar radiation field calculated in Popescu et al. (2017). As shown in Fig.6, the leptonic model can also explain the observed γ -ray emission with a maximum log-likelihood value of -2.17. The derived index of the electrons is $\alpha = 3.05 \pm 0.07$. However, for the IC model the derived energy budget for the relativistic electrons (>2 GeV) is as high as $(1.1 \pm 0.3) \times 10^{50}$ erg, which is almost 10% of the typical kinetic energy of a supernova explosion 10^{51} erg. The total kinetic energy supplied by the stellar wind from a single massive star within ~ 1 Myr, is $\sim 3 \times 10^{48}$ erg (Ezoe et al. 2006). Since CNC contains > 66 OB stars, the stellar wind power produced by the CNC $> 2 \times 10^{50}$ erg. If we consider the different clusters i.e. Tr 14 (20 OB stars), Tr 16 (21 OB stars) (Shull et al. 2021) and NGC 3324 (20 OB stars) (Bisht et al. 2021), we evaluate the stellar wind power 6×10^{49} erg, 6.3×10^{49} erg and 6×10^{49} erg, respectively.

5 CR CONTENT IN THE VICINITY OF THE CNC

The spatial distributions of CRs can provide key information about their injection history. In Westerlund 1, Cygnus Cocoon (Aharonian et al. 2019), and Westerlund 2 (Yang et al. 2018), the $1/r$ CR profiles are derived, which implies the continuous injection and diffusion dominated propagation of CRs from these massive star clusters (Yang & Liu 2022).

We study the propagated CR contents in the vicinity of CNC.

Because of the limited angular resolution and size of this region, we chose only region A and region B, rather than annuli to derive the CR density. In both regions, the gamma-ray flux above 5 GeV and gas mass are derived separately. For gas content, the results of spatial analysis in Sect. 2.4 have shown that the γ -ray emission region has good spatial consistency with the $H_2 + H\text{II}$ template. Thus, we derived the corresponding gas mass for regions A and B, respectively. Then we calculated CR density according to the function (A.4) in Huber et al. (2013). The derived CR density from the two γ -ray emission regions and gas distributions are shown in Fig. 7. The first red point is related to region A and the second one is related to region B. As mentioned in Aharonian et al. (2019), the radial distribution of the CR density in the form,

$$w(r) = w_0(r/r_0)^{-1} \quad (6)$$

where r_0 is assumed to be 10 pc, i.e. normalise the CR proton density w_0 outside but not far from the cluster. The total energy of CR protons within the volume of the radius R_0 is

$$W_p = 4\pi \int_0^{R_0} w(r)r^2 dr \approx 2.7 \times 10^{47} (w_0/1 \text{ eV/cm}^3)(R_0/10 \text{ pc})^2 \text{ erg}. \quad (7)$$

The derived CR profile is shown in the Fig. 7. We fit the density profile using a $1/r$ type distribution, which would result from a continuous injection of CRs from region A. We found no $1/r$ dependence and the CR density of region B is significantly lower than that of region A. For such a profile, the CR content in this system are indeed from some recent impulsive process rather than continuous injections. Certainly, here we note the recent studies have shown that the CR radial profiles for Westerlund 1 (Aharonian et al. 2022) and Cygnus Cocoon (Abeyssekara et al. 2021) are not compatible with $1/r$. Moreover, from a theoretical point of view, the $1/r$ profile is not the only possible outcome for the case of a steady central source. Actually, flatter spatial profiles are more favoured in the case of acceleration by the termination shock of stellar winds (Morlino et al. 2021).

6 DISCUSSION AND CONCLUSION

In this paper we analyze the γ -rays emission from the massive star forming region of CNC. We found that the γ -ray emission in this region can be resolved into three components. Besides the point-like source coincides with the massive binary η Car, we further found two diffuse γ -ray emission components that are spatially correlated with the molecular and ionized gas.

The γ -ray emission from the CNC (region A) can be modelled by a Gaussian disk with radius of 0.4° . The spectral of this component can be described by a broken power-law function with an index of 2.36 ± 0.01 . The spectrum shape of region A reveals a significant pion-bump feature, which indicates the γ -ray emissions are from the interaction of hadronic CRs with ambient gas. However, compared with the γ -ray emissions from other YMCs, the spectrum is significantly softer but is similar to the spectral shape of the Galactic diffuse emission and the emissions from η Car itself. So it is possible the derived emission in this region are still significantly contaminated by the η Car which is by far brighter. Another possibility is that the CO gas and $H\text{II}$ gas in this region are illuminated by the soft CR component accelerated by the η Car. In the latter, the derived W_p is 10^{48} erg for the protons above 2 GeV, considering wind power of the η Car of 10^{38} erg/s and a acceleration efficiency

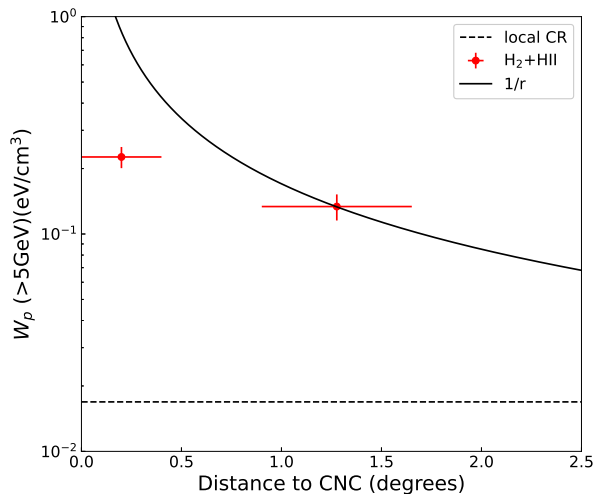


Figure 7. Derived CR density profile near the CNC. The data points are the γ -ray emission above 5 GeV of the CNC. The solid curve is the $1/r$ profile, which is predicted by the continuous injection. For details, see the context in Sect. 5.

of 10%. The CR injection power can be $P_{\text{CR}} \sim 10^{37}$ erg/s. Taking into account the size of region A of about $l = 15$ pc (0.4° in 2.3 kpc), the required diffusion coefficient in this region can be estimated as $D \sim \frac{l}{4T}$, where the confinement time T can be estimated as $W_p/P_{\text{CR}} \sim 10^{11}$ s. The derived D is 5×10^{27} cm²/s, which is one order of magnitude smaller than the average value in the galactic plane. Such a suppression of diffusion coefficient is also found in other regions near CR source (Aharonian et al. 2019). We note that other than η Car other massive stars in the young massive cluster Tr14 and Tr 16 may also accelerate CRs, which will loose our constraints on the diffusion coefficient.

The GeV γ -ray emission from the northern part of the CNC (region B) can be modelled as a 0.75° Gaussian disk. The γ -ray emission has a hard spectrum with a spectral index of about 2.12 ± 0.02 . Although the spectrum of region B can be fit by both leptonic and hadronic scenarios, the high gas density and good spatial correlation between γ -ray emission and molecular gas strongly favor a hadronic origin. In this case the hard γ -ray spectrum and the hard spectrum of parent CRs are similar to those in other YMC systems. A natural acceleration site of the CRs are the YMC Tr 14 and Tr 16, in this case we plot the radial distribution of CRs in region A and region B, which we found are not consistent with the $1/r$ distributions measured near other YMCs (Aharonian et al. 2019). One possible explanation may be that the CR content in this system are indeed from some recent impulsive process rather than continuous injections. In this case the harder spectrum in region B compared with region A can also be explained as energy dependent propagation. Another possibility is that it is the young star cluster NGC 3324 or other unknown CR sources, rather than Tr14 and Tr 16, that accelerate the CRs in region B. Then the different spectrum in region A and region B can be attributed to the different CR injection spectrum in two systems. Indeed, in Yang et al. (2018) the diffuse emission in this region are attributed to the CRs accelerated by the YMC Westerlund 2, which locates about 5 kpc from the solar system. We note that after the detailed analysis in this paper we still cannot formally rule out such a possibility, although the projection distance of region B are significantly nearer with respect to η Car and Tr14/Tr16. The gas distribution derived near Westerlund 2 also reveal a peak in coincidence with region B (Yang et al. 2018). In-

deed the speed interval used in CNC ($v_{\text{LSR}} = [-32, -5] \text{ km s}^{-1}$) and Westerlund 2 ($v_{\text{LSR}} = [-11, 20] \text{ km s}^{-1}$) are overlapped with each other, although their distance to the solar system are significantly different. More detailed studies on the gas distributions in this region may be required to pin down the origin of the diffuse γ -ray emissions in this region.

7 ACKNOWLEDGEMENTS

This work is supported by the National Natural Science Foundation of China (Grant No. 12133003, 12103011, and U1731239), Guangxi Science Foundation (grant No. AD21220075). Rui-zhi Yang is supported by the NSFC under grants 11421303, 12041305 and the national youth thousand talents program in China.

8 DATA AVAILABILITY

The *Fermi*-LAT data used in this work is publicly available, which is provided online by the NASA-GSFC Fermi Science Support Center⁶. We make use of the CO data⁷ to derive the H₂. The data from *Planck* legacy archive⁸ are used to derive the H I. The H I data are from the HI4PI⁹.

REFERENCES

- Abdo A. A., et al., 2009a, *ApJS*, **183**, 46
 Abdo A. A., et al., 2009b, *ApJ*, **706**, L1
 Abdollahi S., et al., 2020, *ApJS*, **247**, 33
 Abeyssekara A. U., et al., 2021, *Nature Astronomy*, **5**, 465
 Abramowski A., et al., 2012, *A&A*, **537**, A114
 Ackermann M., et al., 2011, *Science*, **334**, 1103
 Ackermann M., et al., 2017, *ApJ*, **843**, 139
 Aguilar M., et al., 2015, *Phys. Rev. Lett.*, **114**, 171103
 Aharonian F., et al., 2007, *A&A*, **467**, 1075
 Aharonian F., Yang R., de Oña Wilhelmi E., 2019, *Nature Astronomy*, **3**, 561
 Aharonian F., et al., 2022, arXiv e-prints, p. arXiv:2207.10921
 Akaike H., 1974, *IEEE Transactions on Automatic Control*, **19**, 716
 Ascenso J., Alves J., Vicente S., Lago M. T. V. T., 2007, *A&A*, **476**, 199
 Baade W., Zwicky F., 1934, *Proceedings of the National Academy of Science*, **20**, 259
 Balbo M., Walter R., 2017, *A&A*, **603**, A111
 Ballet J., Burnett T. H., Digel S. W., Lott B., 2020, arXiv e-prints, p. arXiv:2005.11208
 Bisht D., Zhu Q., Yadav R. K. S., Ganesh S., Rangwal G., Durgapal A., Sariya D. P., Jiang I.-G., 2021, *MNRAS*, **503**, 5929
 Bolatto A. D., Wolfire M., Leroy A. K., 2013, *ARA&A*, **51**, 207
 Bykov A. M., Ellison D. C., Gladilin P. E., Osipov S. M., 2015, *MNRAS*, **453**, 113
 Dame T. M., Hartmann D., Thaddeus P., 2001, *ApJ*, **547**, 792
 Daminieli A., et al., 2008, *MNRAS*, **384**, 1649
 Danilenko A., Kirichenko A., Sollerman J., Shibano Y., Zyuzin D., 2013, *A&A*, **552**, A127
 De Becker M., Raucq F., 2013, *A&A*, **558**, A28
 Del Valle M. V., Romero G. E., 2012, *A&A*, **543**, A56
 Ezoë Y., Kokubun M., Makishima K., Sekimoto Y., Matsuzaki K., 2006, *ApJ*, **638**, 860
 Farnier C., Walter R., Leyder J. C., 2011, *A&A*, **526**, A57
 Finkbeiner D. P., 2003, *ApJS*, **146**, 407
 Fujita S., et al., 2021, *PASJ*, **73**, S201
 Göppel C., Preibisch T., 2022, arXiv e-prints, p. arXiv:2201.09097
 Gupta N., Razzaque S., 2017, *Phys. Rev. D*, **96**, 123017
 H. E. S. S. Collaboration et al., 2011, *A&A*, **525**, A46
 H. E. S. S. Collaboration et al., 2020, *A&A*, **635**, A167
 HESS Collaboration et al., 2012, *MNRAS*, **424**, 128
 H.E.S.S. Collaboration et al., 2015, *Science*, **347**, 406
 HI4PI Collaboration et al., 2016, *A&A*, **594**, A116
 Hamaguchi K., et al., 2007, *PASJ*, **59**, 151
 Hamaguchi K., et al., 2018, *Nature Astronomy*, **2**, 731
 Hillier D. J., Davidson K., Ishibashi K., Gull T., 2001, *ApJ*, **553**, 837
 Huber B., Tchernin C., Eckert D., Farnier C., Manalaysay A., Straumann U., Walter R., 2013, *A&A*, **560**, A64
 Jean P., Cheung C. C., Ojha R., van Zyl P., Angioni R., 2018, *The Astronomer's Telegram*, **11546**, 1
 Kafexhiu E., Aharonian F., Taylor A. M., Vila G. S., 2014, *Phys. Rev. D*, **90**, 123014
 Kelner S. R., Aharonian F. A., Bugayov V. V., 2006, *Phys. Rev. D*, **74**, 034018
 Khangulyan D., Aharonian F. A., Kelner S. R., 2014, *ApJ*, **783**, 100
 Lande J., et al., 2012, *ApJ*, **756**, 5
 Lebrun F., et al., 1983, *ApJ*, **274**, 231
 Liu B., Yang R.-z., 2022, *A&A*, **659**, A101
 Liu B., Yang R.-z., Chen Z., 2022, arXiv e-prints, p. arXiv:2205.06430
 Martí-Devesa G., Reimer O., 2021, *A&A*, **654**, A44
 Mestre E., et al., 2021, *MNRAS*, **505**, 2731
 Morlino G., Blasi P., Peretti E., Cristofari P., 2021, *MNRAS*, **504**, 6096
 Ohm S., Zabalza V., Hinton J. A., Parkin E. R., 2015, *MNRAS*, **449**, L132
 Parkin E. R., Pittard J. M., Corcoran M. F., Hamaguchi K., Stevens I. R., 2009, *MNRAS*, **394**, 1758
 Pittard J. M., Corcoran M. F., 2002, *A&A*, **383**, 636
 Planck Collaboration et al., 2016, *A&A*, **594**, A10
 Popescu C. C., Yang R., Tuffs R. J., Natale G., Rushton M., Aharonian F., 2017, *MNRAS*, **470**, 2539
 Preibisch T., et al., 2011, *A&A*, **530**, A34
 Preibisch T., Fleischlen S., Gaczkowski B., Townsley L., Broos P., 2017, *A&A*, **605**, A85
 Rebollo D., Green A. J., Burton M. G., Breen S. L., Garay G., 2021, *ApJ*, **909**, 93
 Reitberger K., Reimer A., Reimer O., Takahashi H., 2015, *A&A*, **577**, A100
 Seo Y. M., et al., 2019, *ApJ*, **878**, 120
 Shull M., Darling J., Danforth C., 2021, arXiv e-prints, p. arXiv:2103.07922
 Smith N., 2006, *MNRAS*, **367**, 763
 Smith N., 2008, *Nature*, **455**, 201
 Smith N., Brooks K. J., 2007, *MNRAS*, **379**, 1279
 Smith N., Egan M. P., Carey S., Price S. D., Morse J. A., Price P. A., 2000, *ApJ*, **532**, L145
 Sodroski T. J., Odegard N., Arendt R. G., Dwek E., Weiland J. L., Hauser M. G., Kelsall T., 1997, *ApJ*, **480**, 173
 Sun X.-N., Yang R.-Z., Wang X.-Y., 2020a, *MNRAS*, **494**, 3405
 Sun X.-N., Yang R.-Z., Liang Y.-F., Peng F.-K., Zhang H.-M., Wang X.-Y., Aharonian F., 2020b, *A&A*, **639**, A80
 Sun X.-N., Yang R.-Z., Liang E.-W., 2022, *A&A*, **659**, A83
 Tavani M., et al., 2009, *ApJ*, **698**, L142
 Vallée J. P., 2014, *ApJS*, **215**, 1
 Verner E., Bruhweiler F., Gull T., 2005, *ApJ*, **624**, 973
 White R., Breuhaus M., Konno R., Ohm S., Reville B., Hinton J. A., 2020, *A&A*, **635**, A144
 Yang R.-z., Aharonian F., 2017, *A&A*, **600**, A107
 Yang R.-Z., Liu B., 2022, *Science China Physics, Mechanics, and Astronomy*, **65**, 219511
 Yang R.-z., de Oña Wilhelmi E., Aharonian F., 2018, *A&A*, **611**, A77
 Zabalza V., 2015, in 34th International Cosmic Ray Conference (ICRC2015), p. 922 (arXiv:1509.03319)

⁶ <https://fermi.gsfc.nasa.gov/ssc/data/access/lat/>

⁷ <https://lambda.gsfc.nasa.gov/product/>

⁸ <http://pla.esac.esa.int/pla/#home>

⁹ <http://cdsarc.u-strasbg.fr/viz-bin/qcat?J/A+A/594/A116>

This paper has been typeset from a $\text{\TeX}/\text{\LaTeX}$ file prepared by the author.